

Supplemental Material for – Magnetic behavior of 5d¹ Re-based double perovskite Sr₂ZnReO₆

Muhammad Maikudi Isah¹,¹ Biswajit Dalal^{2,3},^{2,3} Xun Kang,² Dario Fiore Mosca⁴,⁴
 Ifeanyi John Onuorah⁵,⁵ Valerio Scagnoli^{6,7},^{6,7} Pietro Bonfà⁵,⁵ Roberto De Renzi⁵,⁵
 Alexei A. Belik²,² Cesare Franchini,⁴ Kazunari Yamaura^{2,8,*} and Samuele Sanna^{1,†}

¹Dipartimento di Fisica e Astronomia “A. Righi”, Università di Bologna, I-40127 Bologna, Italy

²Research Center for Materials Nanoarchitectonics (MANA),

National Institute for Materials Science (NIMS), Namiki 1-1, Tsukuba, Ibaraki 305-0044, Japan

³Department of Physics, Achhruram Memorial College, Jhalda, Purulia, West Bengal, 723202, India

⁴University of Vienna, Faculty of Physics and Center for Computational Materials Science, Vienna, Austria

⁵Dipartimento di Scienze Matematiche, Fisiche e Informatiche, Università di Parma, I-43124 Parma, Italy

⁶Laboratory for Mesoscopic Systems, Department of Materials, ETH Zürich, Zürich, Switzerland

⁷PSI Center for Neutron and Muon Sciences, 5232 Villigen PSI, Switzerland

⁸Graduate School of Chemical Sciences and Engineering, Hokkaido University,
 North 10 West 8, Kita-ku, Sapporo, Hokkaido 060-0810, Japan

SI. CRYSTAL STRUCTURE

In order to assign the correct space group symmetry for Sr₂ZnReO₆ we tested all the space groups expected for an ordered double perovskite structure, monoclinic and tetragonal. Combined analysis of both monoclinic and tetragonal model yield more accurate results than using either model individually, with monoclinic and tetragonal phase dominant at low and high temperature, respectively. We attempted to analyze the present diffraction data obtained at low temperatures with two monoclinic structural models, i.e. *I*2/*m* (no. 12; Glazer notation *a*⁰*b*[−]*b*[−] [S1]) and *P*2₁/*n* (no. 14; Glazer notation *a*⁺*a*[−]*a*[−] [S1]). At 150 K, there is little difference between the results of *P*2₁/*n* model (*R*_{wp} = 2.7%, *R*_p = 2.0%, χ^2 = 3.10) and that of *I*2/*m* model (*R*_{wp} = 2.6%, *R*_p = 1.9%, χ^2 = 3.02). It should be pointed out that *P*2₁/*n* is the space group most frequently found for the symmetry of the monoclinic perovskites. Therefore, we concluded that Sr₂ZnReO₆ has the structure with *P*2₁/*n* at low temperature. At room temperature, the best-fit refinement of the dominant phase was achieved with *I*4/*m* space group (Glazer notation *a*⁰*b*⁰*c*[−] [S1]). The refined structural parameters are shown in Tab. S1. The conventional unit cell of Sr₂ZnReO₆ at 150 K and room temperature is shown in Fig. S1.

The temperature dependence of the lattice parameters of Sr₂ZnReO₆ is shown in Fig. S2(a-c) while the temperature evolution of selected diffraction peaks is shown in Fig. S2(d).

TABLE S1. Crystallographic parameters for Sr₂ZnReO₆ at 150 K and room temperature [298(2) K]. From left to right: Atomic labels, Wyckoff symbols (“Wyck.”), Site occupancies (“Occ.”), fractional atomic coordinates (*x/a*, *y/b*, *z/c*), and isotropic thermal parameters (*B*_{iso}).

monoclinic at 150 K: spacegroup <i>P</i> 2 ₁ / <i>n</i> (no. 14)							tetragonal at RT: spacegroup <i>I</i> 4/ <i>m</i> (no. 87)						
Atom	Wyck.	Occ.	<i>x/a</i>	<i>y/a</i>	<i>z/a</i>	<i>B</i> _{iso} (Å ²) ^a	Atom	Wyck.	Occ.	<i>x/a</i>	<i>y/a</i>	<i>z/a</i>	<i>B</i> _{iso} (Å ²) ^a
Sr	4 <i>e</i>	1.0	0.989(1)	0.0131(8)	0.2508(5)	0.20(4)	Sr	4 <i>d</i>	1.0	0	0.5	0.25	0.56(3)
Zn	2 <i>c</i>	1.0	0.5	0	0.5	0.01(5)	Zn	2 <i>a</i>	1.0	0	0	0	0.06(6)
Re	2 <i>d</i>	1.0	0.5	0	0	0.27(2)	Re	2 <i>b</i>	1.0	0	0	0.5	0.31(2)
O1	4 <i>e</i>	1.0	0.044(3)	0.538(5)	0.253(2)	0.3	O1	4 <i>e</i>	1.0	0	0	0.256(1)	0.1(1)
O2	4 <i>e</i>	1.0	0.703(3)	0.278(3)	0.00(3)	0.3	O2	8 <i>h</i>	1.0	0.286(2)	0.232(1)	0	0.1(1)
O3	4 <i>e</i>	1.0	0.224(3)	0.200(3)	0.00(3)	0.3							
<i>a</i> = 5.61949(5) Å, <i>b</i> = 5.58271(5) Å, <i>c</i> = 7.89335(7) Å							<i>a</i> = 5.57423(2) Å, <i>b</i> = <i>a</i> , <i>c</i> = 7.9925(7) Å						
β = 90°; <i>V</i> = 247.630(4) Å ³							β = 90°; <i>V</i> = 248.553(3) Å ³						
<i>R</i> _{wp} = 2.7%, <i>R</i> _p = 2.0%; χ^2 = 3.10							<i>R</i> _{wp} = 2.39%, <i>R</i> _p = 1.7%; χ^2 = 5.69						

Note: Additional occupancy refinements at 150 K yielded 1.000(8) Zn + 0.000 Re on the Zn site and 0.999(5) Re + 0.001 Zn on the Re site. Oxygen occupancies refined to *g*(O1) = 0.984(17), *g*(O2) = 1.05(16), and *g*(O3) = 1.05(16). These results indicate no resolvable antisite disorder or oxygen non-stoichiometry within the experimental uncertainty ($\leq 2-3\%$).

^a *B*_{iso} of oxygen atoms were refined together with constraint to yield same value

* yamaura.kazunari@nims.go.jp

† s.sanna@unibo.it

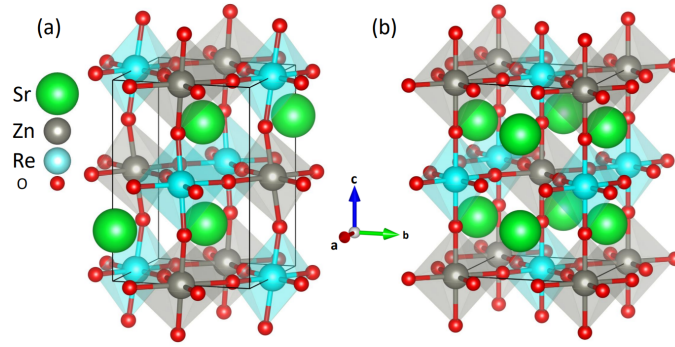


FIG. S1. The crystal structure of $\text{Sr}_2\text{ZnReO}_6$ is depicted in (a) the monoclinic phase at 150 K and (b) the tetragonal phase at room temperature, showing ReO_6 and ZnO_6 octahedra. Green, black, cyan, and red balls denote Sr, Zn, Re, and O, respectively.

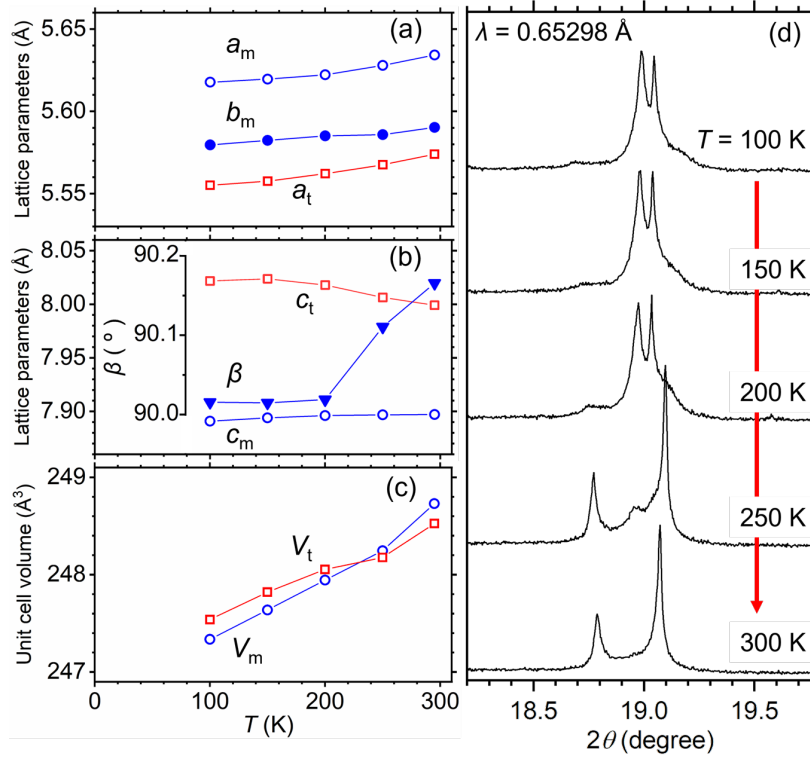


FIG. S2. (a–c) Temperature dependence of the lattice parameters and unit cell volume for both tetragonal and monoclinic $\text{Sr}_2\text{ZnReO}_6$. The lowercase letters “t” and “m” indicate the parameters for the tetragonal and monoclinic phases, respectively. Error bars are omitted for clarity, as they are smaller than the markers. (d) An enlarged view of a section of the synchrotron XRD pattern of $\text{Sr}_2\text{ZnReO}_6$. Measurements were first taken at 100 K and then during the heating process up to room temperature [298(2) K].

TABLE S2. Comparison of single- and two-phase Rietveld refinements of $\text{Sr}_2\text{ZnReO}_6$ over identical data ranges.

T (K)	Model	Phases	N_{par}	R_{wp} (%)	R_p (%)
150	Single	$P2_1/n$	62	3.50	2.30
150	Two	$P2_1/n + I4/m$	78	2.70	2.00
Phase fraction (monoclinic) at 150 K (two-phase): $f_m = 0.87(3)$					
298	Single	$I4/m$	60	3.06	1.94
298	Two	$I4/m + P2_1/n$	75	2.39	1.70
Phase fraction (tetragonal) at 298 K (two-phase): $f_t = 0.76(4)$					

Note: N_{par} denotes the number of refined (free) parameters in the Rietveld model. All refinements used the same instrument profile and background functions. Fits initialized from different structural and peak-shape parameters converged to the same final solution, confirming refinement robustness.

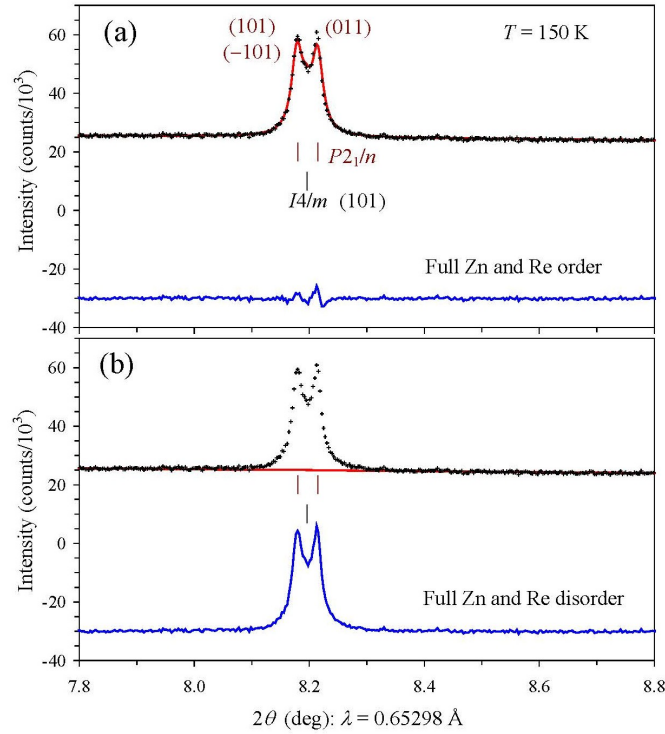


FIG. S3. Antisite-sensitive region of the synchrotron XRD pattern of Sr₂ZnReO₆ at $T = 150$ K and $\lambda = 0.65298$ Å. (a) Refinement with full Zn/Re order (P_{21}/n): observed data (black symbols), calculated profile (red line), and difference (blue line). (b) Test refinement with full Zn/Re disorder, showing a pronounced misfit in intensity and peak shape for the (101)/(101)/(011) features near $2\theta \approx 8.2^\circ$. The comparison demonstrates the refinement sensitivity to Zn/Re ordering.

SII. SUSCEPTIBILITY AND MAGNETIZATION DATA

As shown in Figure S4 both the real [Fig. S4(a)] and imaginary [Fig. S4(b)] components of the ac susceptibility data reveal sharp peaks at ~ 13 K, consistent with T_M observed for the dc susceptibility data. Furthermore, the inset of Figure S4(a) shows the frequency independent nature of the observed peaks, which hints of the absence of any glassy magnetic transition.

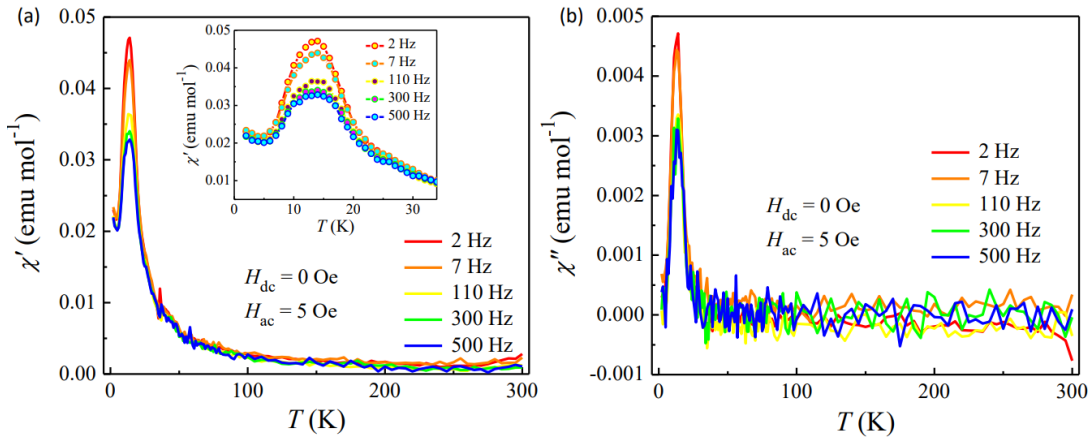


FIG. S4. Temperature dependence of the (a) real [χ'] and (b) imaginary [χ''] component of the ac susceptibility of Sr₂ZnReO₆ with ac field of $H_{ac} = 5$ Oe and at 2, 7, 110, 300 and 500 Hz frequency. The inset show the enlarged view of the real component of the ac susceptibility below 35 K.

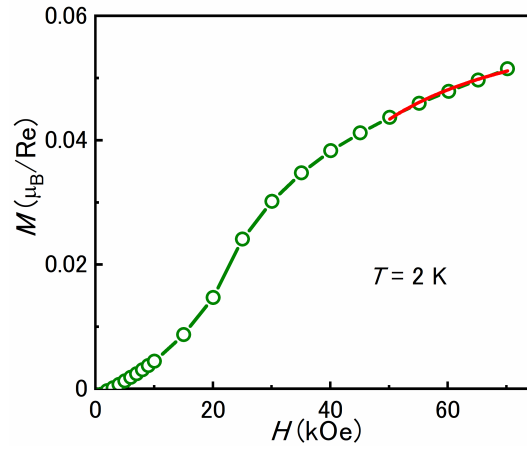


FIG. S5. Law-of-approach-to-saturation (LAS) fit to the high-field region of the $M(H)$ curve for $\text{Sr}_2\text{ZnReO}_6$ at $T = 2$ K. The open green circles represent the experimental data and the red solid line shows the fitted curve using $M(H) = M_S(1 - B/H^2) + \chi H$. The fit yields $M_S = 0.0566 \mu_B/\text{Re}$, slightly higher than the measured value at 70 kOe. The LAS model provides a qualitative estimate of M_S but is not reliable for extracting K in strongly anisotropic systems.

TABLE S3. Curie–Weiss (CW) fits to $\chi(T)$ of $\text{Sr}_2\text{ZnReO}_6$ for different temperature windows. Units: χ_0 in $10^{-4} \text{ emu Oe}^{-1} \text{ mol}^{-1}\text{-Re}$; C in $\text{emu Oe}^{-1} \text{ K mol}^{-1}\text{-Re}$; Θ_{CW} in K; μ_{eff} in μ_B/Re .

Window (K)	χ_0	Θ_{CW} (K)	C / μ_{eff}
100–280	-1.37 ± 0.03	$-20(1)$	$0.072(1) / 0.758(5)$
120–280	-1.31 ± 0.03	$-24(1)$	$0.073(1) / 0.764(1)$
150–280	-1.33 ± 0.06	$-25(4)$	$0.074(2) / 0.769(4)$

Note: $\mu_{\text{eff}} = \sqrt{8C} \mu_B/\text{Re}$. Fits include χ_0 .

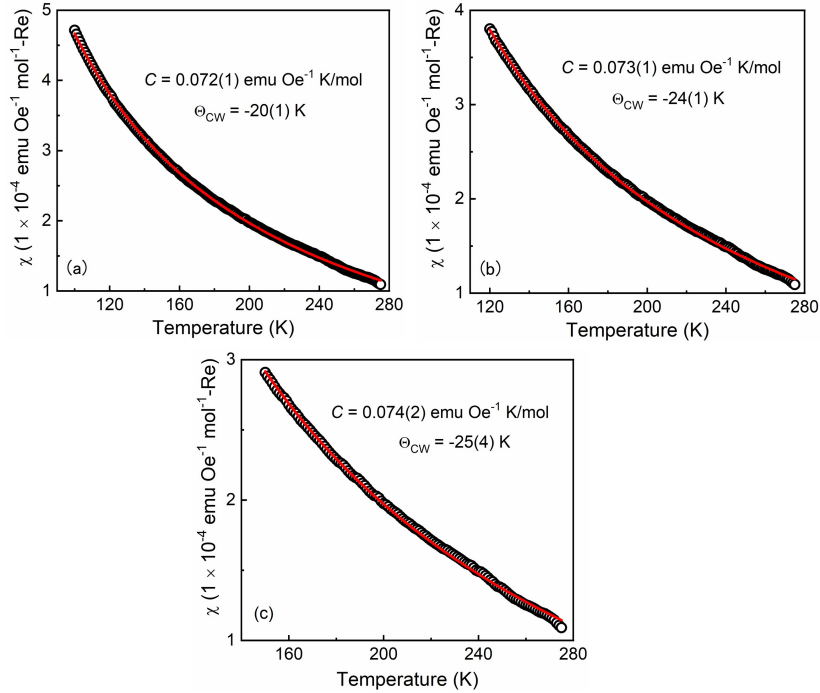


FIG. S6. Curie–Weiss (CW) fits to the magnetic susceptibility of $\text{Sr}_2\text{ZnReO}_6$ over three temperature intervals: (a) 100–280 K, (b) 120–280 K, and (c) 150–280 K. Circles denote experimental data and solid lines represent CW fits including a temperature-independent term χ_0 . The resulting χ_0 , Curie constant (C), Weiss temperature (Θ_{CW}), and effective moment (μ_{eff}) are summarized in Table S3. The close similarity of parameters across different fitting ranges demonstrates the robustness of the Curie–Weiss analysis.

Sensitivity to Re valence impurities. A dilute fraction x of impurity moments modifies the effective moment as $\mu_{\text{eff}}^2 \approx (1-x)\mu_{6+}^2 + x\mu_{\text{imp}}^2$, where μ_{6+} is the moment for Re^{6+} sites and μ_{imp} for the impurity valence. Using $\mu_{6+} \approx 0.76 \mu_B/\text{Re}$ from Table S3: (i) for Re^{5+} ($5d^2$, $\mu_{\text{imp}} \approx 2.83 \mu_B$), keeping μ_{eff} within $\sim 0.01 \mu_B$ of the measured value requires $x \lesssim 0.3\%$; (ii) for Re^{7+} ($5d^0$, $\mu_{\text{imp}} \approx 0$), a $\sim 0.01 \mu_B$ decrease would need $x \gtrsim 2.5\%$. Thus, the CW fits are incompatible with any sizable $\text{Re}^{5+}/\text{Re}^{7+}$ fraction; our synthesis/stoichiometry analysis agrees with this bound.

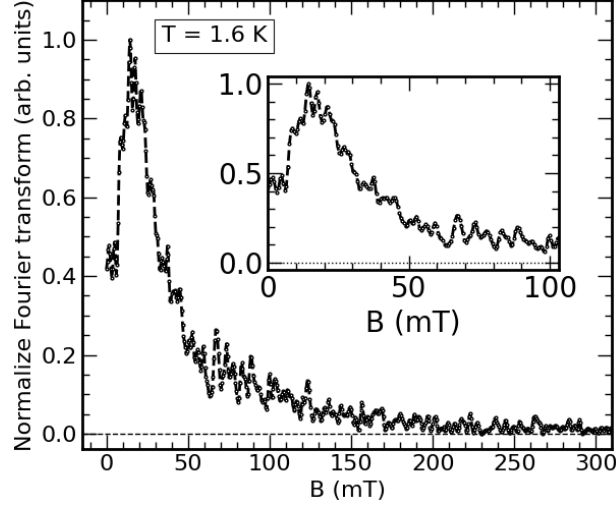


FIG. S7. Normalized Fourier transform of the ZF- μ SR time spectra measured at $T = 1.6$ K [see the main manuscript Fig. 3]. The inset is a zoom view of Fourier transform below 100 mT.

SIIL. μ SR DATA

Figure S7 shows the Fourier-transform of the ZF- μ SR asymmetry data at $T = 1.6$ K used to obtain the probability distribution of the muon local field described in Sec. SIV.

Figure S8 shows the temperature dependence of extracted parameters from fit using Eq. (1) described in the main manuscript.

The μ SR spectra were also measured under longitudinal fields (LF) of $\mu_0 H_{\text{LF}} = 10, 20, 50, 100$, and 200 mT collected at $T = 1.6$ K shown in Fig. S9. With increasing LF, a field of about 200 mT is enough to have a constant asymmetry (full recovery of the muon tail). Since this value is about 10 times the value of the internal field B_μ , the magnetism has static character [S2].

SIV. DIPOLAR SIMULATIONS AND CANTED SPIN MODELS

The total local field at the muon site is approximated by the following contributions: $\mathbf{B} \approx \mathbf{B}_{\text{dip}} + \mathbf{B}_{\text{Lor}}$, where \mathbf{B}_{dip} given by;

$$\mathbf{B}_{\text{dip}} = \frac{\mu_0}{4\pi} \sum_{j=1}^{N_m} \left[\frac{3\mathbf{r}_j(\mathbf{m} \cdot \mathbf{r}_j)}{r_j^5} - \frac{\mathbf{m}_j}{r_j^3} \right], \quad (\text{S1})$$

is the long range dipolar field contribution which is obtained here in real space using the Lorentz method for N_m magnetic moments within the Lorentz sphere and \mathbf{B}_{Lor} is the Lorentz contribution of magnetic moments outside the Lorentz sphere [S3].

Fit procedure: For each magnetic structure, to fit the magnitude of computed local field (B) at $N = 48$ (at the eight muon positions including at their symmetry equivalent positions i.e 48 positions in all) muon sites to the experimental distribution, first the computed local field distribution as a function of Re moments is approximated as:

$$p(B, m_{\text{Re}}) = \sum_{i=1}^N \delta(B - m_{\text{Re}} B_i). \quad (\text{S2})$$

Such that the Fourier-transform distribution of the ZF- μ SR experimental spectra at $T = 1.6$ K can be approximated as a convolution with Gaussian broadening g define as:

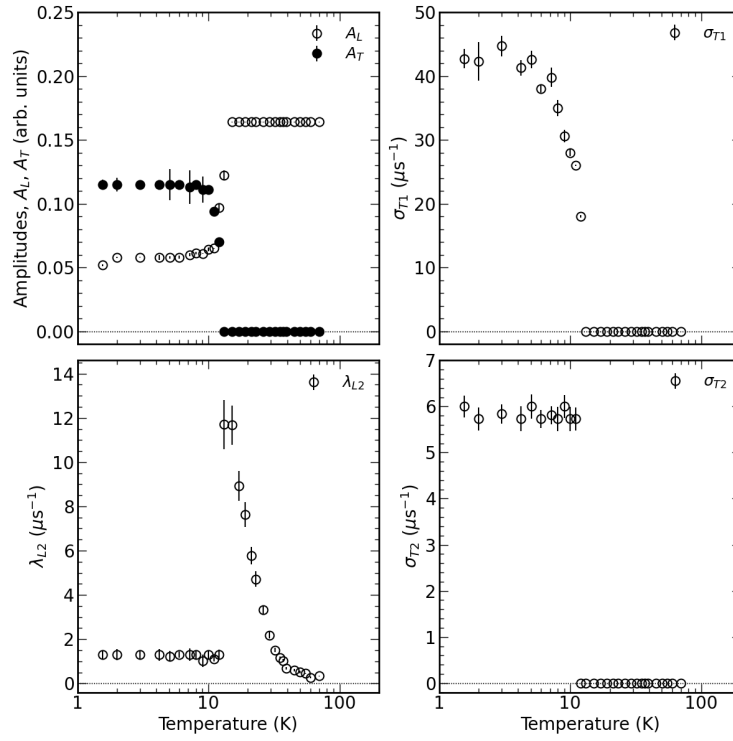


FIG. S8. Temperature dependence of fit parameters obtain from the fit of ZF- μ SR function Eq. (1) described in the main manuscript.

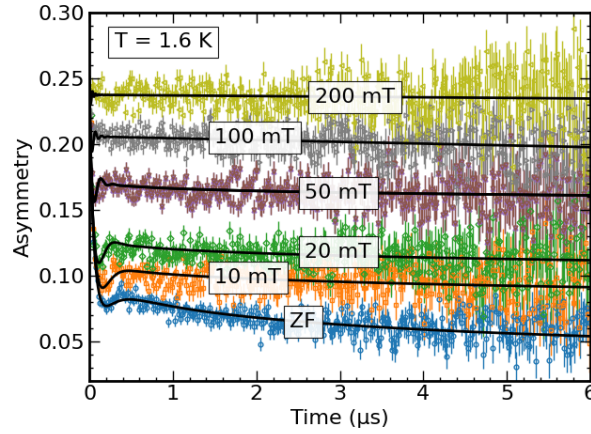


FIG. S9. LF dependence of μ SR spectra at 1.6 K.

$$\tilde{p}(B, m_{\text{Re}}, \sigma) = (p * g)(B) := \int_{-\infty}^{\infty} p(\tau, m) g(B - \tau, \sigma) d\tau. \quad (\text{S3})$$

yielding the fitting function ρ

$$\rho(B; m, \sigma, A) = A\tilde{p}(B, m, \sigma) + A_{\text{bg}}, \quad (\text{S4})$$

where m , σ , A are the magnitude of the Re ordered moment, width and amplitude of the distribution respectively. A_{bg} is a constant background to offset the zero of the distribution.

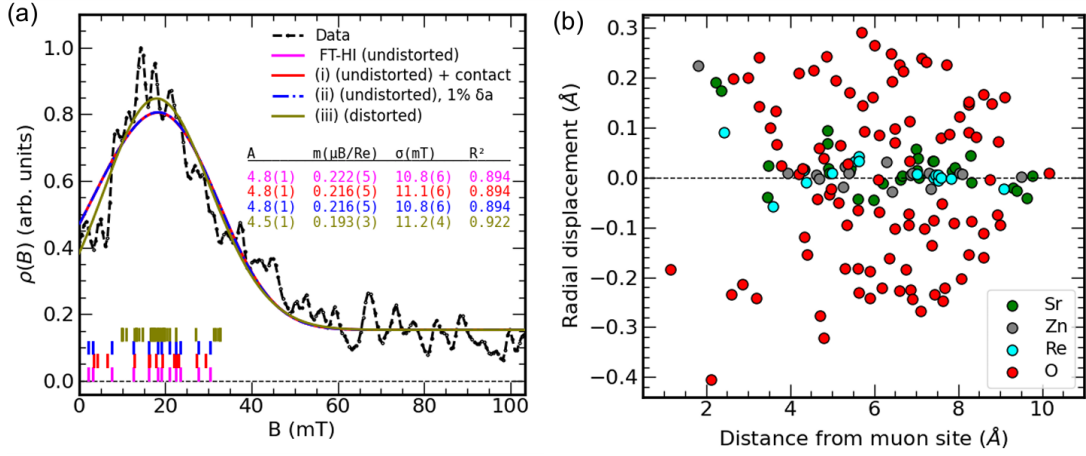


FIG. S10. (a) Comparison between experimental ZF- μ SR field distribution measured at $T = 1.6$ K (black line) and fit of the calculated local field distribution $\rho(B)$ using the proposed magnetic structure (solid colored lines) for the undistorted (solid magenta colored line) and the results of points (i)–(iii). The inset shows the calculated fit parameters. The vertical ticks of same color is the calculated local fields at the muon sites using the magnetic moment obtained from the fit. (b) Radial displacements of the Sr, Zn, Re and O atoms from their equilibrium positions as a function of their distances from a representative muon site A_{II} in $\text{Sr}_2\text{ZnReO}_6$ (see Table I of the main text).

A. Sensitivity of the calculated magnetic moment

In Fig. S10 we show the calculated $\rho(B)$ in the undistorted monoclinic lattice and its sensitivity against the following conditions:

- (i) the contact hyperfine field contribution, for which we assumed values corresponding to 10% of the computed dipolar contribution for each muon site in the monoclinic lattice;
- (ii) the change in lattice parameters as a function of temperature, where, based on x-ray diffraction results [Fig. S2], we assumed a maximum variation of 1% in the monoclinic lattice (δa), between 150 K and 1.6 K; and
- (iii) the effects of the DFT computed muon-induced distortions on the monoclinic lattice.

The results of points (i)–(iii) are presented in the Fig. S10(a), which includes the representative fits and a table containing the key fit parameters. As expected, the computed magnetic moments are robust and vary only slightly with respect to the quantities considered. The most significant effect arises from the muon-induced distortion with obtained moment of $0.193 \mu_B$, as shown in the inset of the figure. As shown in the Fig. S10, the implantation of the muon does not lead to significant distortion of the host carrying magnetic ion Re^{6+} from their equilibrium position, as the maximum displacement remains below 0.1 \AA [Fig. S10(b)] which is the most important for the reported fit. Overall, this check confirms that the estimation of the ordered moment to be $\leq 0.2 \mu_B$.

SV. FORCE-THEOREM IN HUBBARD-I

A. Calculation of Intersite Exchange Interactions

We evaluate the intersite exchange interactions (IEI) in $\text{Sr}_2\text{ZnReO}_6$ using the force-theorem in the Hubbard-I (FT-HI) method derived in Ref. [S4] as publicly available in the GitHub repository [S5]. We incorporate both the electron-mediated IEI and the monoclinic crystal field contribution. The IEI Hamiltonian describing the interactions between multipolar moments with a defined total angular momentum $j_{\text{eff}} = 3/2$, is expressed as

$$H = \sum_{\langle ij \rangle} V_{KK'}^{QQ'}(ij) O_K^Q(i) O_{K'}^{Q'}(j), \quad (\text{S5})$$

where $O_K^Q(i)$ is the multipolar operator acting on the j_{eff} -multiplet on site i of the rank $K = 0 \dots 2J$ and projection $Q = -K \dots K$ [S6]. The first summation $\langle ij \rangle$ runs over the Re-Re bonds and $V_{KK'}^{QQ'}(ij)$ represent the corresponding IEI.

The FT-HI method is based on a converged electronic paramagnetic structure calculation in the quasi atomic (Hubbard-I) approximation. At its core, it considers small symmetry-breaking fluctuations of the density matrix of the ground-state multiplet

occurring simultaneously at two interacting (neighboring) magnetic (Re) sites, i and j . The IEI $V_{KK'}^{QQ'}(ij)$ is then computed by analyzing the response of the DFT+DMFT grand potential to these two-site fluctuations. The approach shares conceptual similarities with other force-theorem approaches developed for symmetry-broken magnetic states [S7, S8], but is designed for the symmetry-unbroken paramagnetic regime, accessible in DFT+DMFT. In the case of $\text{Sr}_2\text{ZnReO}_6$, we follow closely previous application to other $j_{\text{eff}} = 3/2$ double perovskites [S9, S10]. Further details are provided in the Supplemental Material of Ref. [S11], while the full derivation is available in Ref. [S4].

B. Crystal Field in $J_{\text{eff}} = 3/2$ basis

We report the crystal-field matrix $H_{MM'}$ for the Re sites, as computed in the global reference frame and expressed in the $|J = 3/2, m_J\rangle$ basis (see Table S4) following

$$H_{MM'} = \sum_{\Gamma} \langle JM|\Gamma\rangle E_{\Gamma} \langle\Gamma|JM'\rangle \quad (\text{S6})$$

where $|\Gamma\rangle$ are the ground state multiplet eigenstates of the atomic Hamiltonian. Because of the monoclinic symmetry of the lattice, we do not rotate the basis into a local octahedral frame: the tilt of the apical oxygen atoms prevents the definition of an orthonormal Cartesian frame aligned with the oxygens in the ab plane.

The strong mixing between states with different m_J values arises not only from the use of the global reference frame, but also from significant hybridization between the $J_{\text{eff}}=3/2$ ground-state manifold and the excited $J_{\text{eff}}=1/2$ states, as consequence of the large crystal-field splitting of the multiplet.

M	Real				Imaginary			
-3/2	44.4561	-67.9360	-15.2325	0	0	29.8418	1.3137	0
-1/2	-67.9360	129.1068	0	-15.2324	-29.8418	0	0	1.3137
1/2	-15.2325	0	129.1062	67.9358	-1.3137	0	0	-29.8419
3/2	0	-15.2324	67.9358	44.4572	0	-1.3137	29.8419	0

TABLE S4. Crystal Field matrix of Re in the monoclinic crystal field of $\text{Sr}_2\text{ZnReO}_6$

C. Origin of the canted AFM phase

To identify which multipolar channels drive the canted antiferromagnetic phase, we performed a series of mean-field (MF) calculations in which specific intersite exchange interactions were selectively switched off.

The results are summarized in Table S5. They show that the canting angle originates from a cooperative interplay among all time-odd multipolar couplings—dipole–dipole, quadrupole–quadrupole, dipole–octupole, and octupole–octupole. The correct canting angle and magnetic ground state cannot be reproduced by any single interaction channel alone, but only when all are included. This behavior is consistent with findings for other $5d^1$ double perovskites such as $\text{Ba}_2\text{NaOsO}_6$ [S11].

Canting Angle vs Active IEI						
IEI:	All	dd	dd + qq	do + oo	oo	qq
ϕ (degrees)	55	28	28	20	20	no dipoles

TABLE S5. Canting angle (ϕ) dependence on IEI in $\text{Sr}_2\text{ZnReO}_6$. The different interactions are reported as follows: Dipole-Dipole (dd), Dipole-Octupole (do), Quadrupole-Quadrupole (qq) and Octupole-Octupole (oo)

D. Canting angle dependence vs U

We investigated the robustness of the canted antiferromagnetic phase by tuning the U parameter in DFT+HI steps of 0.25 eV from $U = 3.0$ eV to $U = 3.5$ eV. The results are shown in Table S6. We find for each value the same canted AFM configuration, with similar values of the canting angle. The small difference can be a consequence of the precision of the MF. We recall, that the values of the magnetic moments are very small $\sim 0.06\mu_B$, and therefore, small variation of components are expected.

Canting Angle vs U

U (eV)	3.0	3.25	3.5
ϕ (degrees)	56	55	60

TABLE S6. Canting angle (ϕ) dependence on IEI in $\text{Sr}_2\text{ZnReO}_6$. The different interactions are reported as follows: Dipole-Dipole (dd), Dipole-Octupole (do), Quadrupole-Quadrupole (qq) and Octupole-Octupole (oo)

-
- [S1] P. M. Woodward, Octahedral Tilting in Perovskites. I. Geometrical Considerations, *Acta Crystallographica Section B* **53**, 32 (1997).
- [S2] A. Yaouanc and P. Dalmas de Réotier, *Muon Spin Rotation, Relaxation, and Resonance: Applications to Condensed Matter* (Oxford University Press, Oxford, 2011).
- [S3] P. Bonfà, I. J. Onuorah, and R. D. Renzi, Introduction and a Quick Look at MUESR, the Magnetic Structure and mUon Embedding Site Refinement Suite, in *Proceedings of the 14th International Conference on Muon Spin Rotation, Relaxation and Resonance ($\mu\text{SR}2017$)*, Vol. 21 (2018).
- [S4] L. V. Pourovskii, Two-site fluctuations and multipolar intersite exchange interactions in strongly correlated systems, *Phys. Rev. B* **94**, 115117 (2016).
- [S5] L. V. Pourovskii and D. Fiore Mosca, MagInt, <https://github.com/MagInteract/MagInt>.
- [S6] P. Santini, S. Carretta, G. Amoretti, R. Caciuffo, N. Magnani, and G. H. Lander, Multipolar interactions in f -electron systems: The paradigm of actinide dioxides, *Rev. Mod. Phys.* **81**, 807 (2009).
- [S7] A. Liechtenstein, M. Katsnelson, V. Antropov, and V. Gubanov, Local spin density functional approach to the theory of exchange interactions in ferromagnetic metals and alloys, *Journal of Magnetism and Magnetic Materials* **67**, 65 (1987).
- [S8] M. I. Katsnelson and A. I. Liechtenstein, First-principles calculations of magnetic interactions in correlated systems, *Phys. Rev. B* **61**, 8906 (2000).
- [S9] D. Fiore Mosca, C. Franchini, and L. V. Pourovskii, Interplay of superexchange and vibronic effects in the hidden order of $\text{Ba}_2\text{MgReO}_6$ from first principles, *Phys. Rev. B* **110**, L201101 (2024).
- [S10] D. Fiore Mosca and L. V. Pourovskii, Antiferro octupolar order in the $5d^1$ double perovskite $\text{Sr}_2\text{MgReO}_6$ and its spectroscopic signatures, *Phys. Rev. Res.* **7**, L032016 (2025).
- [S11] D. Fiore Mosca, L. V. Pourovskii, B. H. Kim, P. Liu, S. Sanna, F. Boscherini, S. Khmelevskyi, and C. Franchini, Interplay between multipolar spin interactions, Jahn-Teller effect, and electronic correlation in a $J_{\text{eff}} = \frac{3}{2}$ insulator, *Phys. Rev. B* **103**, 104401 (2021).